

HANDBOOK OF BIOLOGICAL CONFOCAL MICROSCOPY

SECOND EDITION

**Edited by
James B. Pawley**

Zoology Department
University of Wisconsin-Madison
Madison, Wisconsin

PLENUM PRESS • NEW YORK AND LONDON

Light Microscopic Images Reconstructed by Maximum Likelihood Deconvolution

Timothy J. Holmes, Santosh Bhattacharyya, Joshua A. Cooper, David Hanzel, Vijaykumar Krishnamurthi, Wen-chieh Lin, Badrinath Roysam, Donald H. Szarowski, and James N. Turner

INTRODUCTION

Overview

The main purpose of this chapter is to introduce the reader to the methodology of maximum likelihood (ML)-based deblurring algorithms. It is aimed at the interdisciplinary scientist, who may not be concerned about the underlying mathematical foundations of the methodology but who needs to understand the main principles behind the algorithms used. Some mathematical principles are explained, but the interested reader may find more details in the numerous publications cited in Holmes (1989, 1992), Krishnamurthi *et al.* (1992), and Shaw and Rawlins (1991). A sample image reconstruction is presented from each of three microscope modalities, including the **wide-field epifluorescence (WFF)** microscope, the **confocal pinhole laser-scanned epifluorescence** microscope (CLSM), and the **transmitted light brightfield (BF)** microscope.

The main advantages of the methodology are discussed, as well as present limitations and expected realistic future developments. Discussions on the origins of the methodology may be found in the references given above. The method is an adaptation from nuclear medicine imaging (Shepp and Vardi, 1982), although both independently and previously, a similar general algorithm was developed under much different mathematical foundations by Richardson (1972) and Lucy (1974). The idea of refining these earlier approaches to accommodate a blind deconvolution, the purpose of which will be discussed, was inspired by the research of Ayers and Dainty (1988).

Purpose of Deblurring

For the WFF and BF microscopes, 3D data may be collected by using the standard optical sectioning technique (Agard, 1984; Chapter 13, *this volume*). This technique involves an automatic

focus controller, in which sequential images of a thick specimen are digitized and stored. This focus controller may employ stepper motors (e.g., AutoQuant, Troy, NY) or piezo crystals embedded within a customized objective lens assembly (e.g., Scanalytics, Bellerica, MA). The microscope, having a depth-of-field (DOF) of $\approx 0.4 \mu\text{m}$ (Martin and Johnson, 1931), is focused on a plane, which may be anywhere from a few microns (e.g., chromosomes or epithelial cells) to 50–200 μm inside the specimen (e.g., neurons or brain slices). This image will contain both sharp in-focus features originating from the plane of focus and blurred features originating from out-of-focus planes either above or below the plane of focus. After storing a single image frame, the microscope is automatically focused to an adjacent plane, which is about one DOF away, and a second image is then digitized. This process is repeated until the entire specimen has been scanned. Although the resulting data set will be a 3D data set, or 3D image, it will be a rather poor image, because it will still contain the out-of-focus blur. It is the purpose of deblurring algorithms to remove this blurred data and to retain only the sharpness and clarity of the original specimen. After doing so, the image may be rendered for 3D viewing and quantitation by methodologies such as those discussed in Chapters 13 and 14.

For the CLSM, images of adjacent planes are sequentially optically sectioned and digitized in a similar way, except that each frame is collected by way of a raster-scanned laser spot and a photomultiplier tube (PMT) pinhole detector. Each confocal image is, by itself, already relatively deblurred in the sense that the confocal imaging method rejects most of the out-of-focus light. Details of this principle are discussed elsewhere in this book. Most of the features that remain in a confocal 3D data set are in-focus features. In spite of this improvement over the WFF microscope, however, the CLSM has its own limitations.

- While it indeed rejects **most** of the out-of-focus light, it by no means rejects **all** of it, and an obvious haze remains,

Timothy J. Holmes, Wen-chieh Lin, Badrinath Roysam, and James N. Turner • Biomedical Engineering Department and Center for Image Processing Research, Rensselaer Polytechnic Institute, Troy, New York 12180-3590; and Wadsworth Center for Laboratories and Research, New York State Department of Health, Albany, New York 12201-0509. Santosh Bhattacharyya, Joshua A. Cooper, and Vijaykumar Krishnamurthi • Biomedical Engineering Department and Center for Image Processing Research, Rensselaer Polytechnic Institute, Troy, New York 12180-3590. Donald H. Szarowski • Wadsworth Center for Laboratories and Research, New York State Department of Health, Albany, New York 12201-0509. David Hanzel • Molecular Dynamics, 880 E. Arques Avenue, Sunnyvale, California 94086. *Present address for VK:* Center for Light Microscope Imaging and Biotechnology, Carnegie Mellon University, Pittsburgh, Pennsylvania 15213.

even though this haze is much reduced from that of the WFF microscope.

- In addition, the image retains substantial axial smearing. For an image that is not diffraction limited, this appears as a linear motion blur in the axial direction. For an image that is diffraction-limited, as with empty magnification (see Chapter 4, *this volume*), this appears as a substantial anisotropy in the spatial resolution, with most of the smearing along the axial direction.
- Because out-of-focus blur is rejected, far fewer photons are detected, so the raw data may contain a substantial quantum-photon noise component. This quantum noise often limits the effectiveness of deconvolution protocols when very fine structures need to be seen. For instance, it limits our ability to detect the small voids in the fluorescence concentration that characterize microelectrode impalement sites (Turner *et al.*, 1991), and it limits our ability to detect dendritic spines. In the case of CLSM, the purpose of deblurring algorithms is to reduce, at least partially, all three of these undesirable effects and thereby to improve the accuracy of the image finally displayed.

Main Advantages and Present Limitations

The most obvious practical advantage of this particular approach to deblurring is that it has a **blind deconvolution** variation. Blind deconvolution is a term used to describe methods of deconvolution that do not require the point-spread function (PSF) of the system to be explicitly known prior to the deconvolution. Instead, a reconstructed estimate of the PSF is produced concurrently with the deblurred image data. What makes this feasible is that we are able to apply some rather powerful, yet realistic, constraints on the PSF solution. What makes this worthwhile is that it eliminates the necessity of measuring the PSF (Hiraoka *et al.*, 1990), a process that is not straightforward for routine usage, which has impeded wide usage of deblurring algorithms. Determining the PSF requires collecting a 3D image of a subresolution fluorescent microsphere, a process complicated by photobleaching of the sphere and statistical noise due to low light levels. In addition, the actual PSF will be degraded by any heterogeneity in the refractive index of the biological specimen (Gibson and Lanni, 1991). These complications are compounded with the confocal microscope, where light levels are especially low and the effect of refractive index even more severe (Visser *et al.*, 1992; Chapter 20, *this volume*). Clearly, an algorithm that will work reliably for those cases in which the PSF cannot be measured would be very useful. It would be even better if such an algorithm could also be applied to 3D BF images made with transmitted light, as this would provide a realistic means to obtain 3D images of absorbing stains.

A third advantage of this approach is that it reduces the apparent noise in the image. We think this is partly because its mathematical foundations have quantum photon noise as a fundamental assumption. Intuitively, this may be explained in the following way. The microscope represents a bandlimited system. As explained later, this means that any "good" signal will lie only inside the bandlimit. Much of the "undesirable" noise energy lies outside the bandlimit, and the algorithm recognizes this and subsequently rejects the "out-of-band" noise automatically. It also constrains the deblurred image to have only non-negative values,

a process that cannot be implemented with a simple bandlimiting filter.

These advantages are most apparent when data are significantly "oversampled." In other words, best results are achieved when the pixel or optical section spacing is finer than required by Nyquist sampling (Chapters 2 and 4, *this volume*).

An earlier, "nonblind" version of this algorithm is referred to as "the accelerative form of the nonblind algorithm," which is relatively fast in execution (Holmes and Liu, 1991), resulting in useful deblurred images within 50 iterations (see Table 1). Because the present, blind version has not yet been accelerated, it is much slower and requires ~500 iterations to produce a comparable image. We are currently developing an accelerated blind version.

PRINCIPLES

Simplified Data Collection Model

The modeling of the data collection process for the WFF and confocal fluorescence microscopes is summarized by the following equations:

$$\mu_n(x,y,z) = \mu_r(x,y,z) + N(x,y,z) \quad (1)$$

and

$$\mu_r(x,y,z) = \mu(x,y,z) + b(x,y,z) \quad (2)$$

TABLE 1. Processing Times and Memory Requirements for Implementation on an Alacron (Nashua, NH) i860 Accelerator Card (FT200-AT-16-1) for PC-Compatible Computers.

3D Image size	Algorithm version ^b	Memory size required (Mbytes)	Iteration No.	Processing time ^c (min)
128 × 128 × 64	Nonblind and nonaccelerated	16	50	3
			100	6
			500	30
	Nonblind and accelerated	32	50	5
			100	10
			500	50
	Blind and nonaccelerated	32	50	6
			100	12
			500	60

^aTimes shown are based on the manufacturer's specification of real-to-complex FFT timing. The nonblind nonaccelerated and nonblind accelerated versions are described elsewhere (Holmes and Liu, 1991; Krishnamurthi *et al.*, 1994 and references cited therein).

^bThe algorithms have also been implemented on an IBM ES9000 mainframe with a vector processor.

^cThe processing times measured with the ES9000 are ~2 times those shown for the i860 card. Requirements for larger or smaller 3D image sizes can be calculated from this table as follows: the memory size must be directly proportional to the 3D image size. Processing time will be proportional to $M \log M$, with M the number of voxels in the 3D image, because this is the proportionality of an FFT operation (Oppenheim and Schaffer, 1975) and most of the processing time is taken up by FFT operations.

where x and y are the in-plane (transverse) spatial variables, z is the axial spatial variable, $b(x,y,z)$ is a background level primarily due to dark current (Janesick *et al.*, 1987; Snyder *et al.*, 1993), $b()$ is equivalent to $\mu_0()$ used by us in previous work), $N()$ is a random noise component, primarily due to quantum photons, and where

$$\mu(x,y,z) = \lambda(x,y,z) * h(x,y,z) \quad (3)$$

with $\lambda()$ the fluorescence dye concentration, and $h()$ the PSF. More comprehensive and precise modeling of this system as a Poisson-random-point process may be found in previous publications (Holmes, 1992; Snyder *et al.*, 1993).

The convolution with $h()$, denoted by $*$, represents the blur in the image. The purpose of the deblurring algorithm is to produce an estimate, or reconstruction, of $\lambda()$. The background level $b(x,y,z)$ is measured in a calibration protocol, discussed later. It is accounted for in the image reconstruction algorithm either by pre-correcting the raw data, by subtracting it from the data (Chapter 13, *this volume*) or by incorporating it within each algorithm iteration.

Maximum Likelihood General Principles

Maximum likelihood estimation (MLE) is a mathematical/computational optimization strategy (Van Trees, 1968) generally used for producing estimates of quantities corrupted by some form of random noise. In a heuristic (Bayesian) interpretation of MLE, one might think of the collected image data as a random quantity having a certain likelihood of being produced among a host of other possible random quantities. This randomness is due to the statistical nature of the quantum photon emissions. The strategy is to produce the estimate of $\lambda()$ that has the highest likelihood of having given rise to the specific data collected.

In mathematical terms, for the classical interpretation, we are formulating a **log-likelihood function** that represents a measure of the likelihood that one would collect the noisy data that were actually collected. This function is actually a functional (i.e., a function of a function) of $\lambda()$, $h()$, and $\mu_n()$. Its derivation is based on the random Poisson nature of the quantum photon noise. In principle, this functional is solved for its maximum value. In blind deconvolution, specific quantities of $\lambda()$ and $h()$ are solved for this maximum, using an iterative search scheme (Dempster *et al.*, 1977). Assuming convergence of the iterations, the specific quantities of $\lambda()$ and $h()$ that solve this maximum become the reconstructed image and the reconstructed PSF, respectively. With the more conventional nonblind deconvolution, $h()$ is assumed to be known from prior measurement, and the deblurring algorithm is solved only for $\lambda()$.

General Flowchart

The general flowchart for the blind deconvolution algorithm is summarized in Fig. 1. In step 1, first guesses of the dye concentration $\lambda^{(0)}()$ and the PSF $h^{(0)}()$ are made, as discussed later in the section on Image Reconstructions. Step 2 is designed from the optimization strategy specified by the expectation-maximization (EM) algorithm (Dempster *et al.*, 1977; Holmes, 1992).

In order to avoid artifacts caused by circular convolution, we place a border around the six faces of the 3D data space. Within these border regions, the data are considered to be truncated for

modeling purposes, as discussed later. For the indices of (x,y,z) that lie inside this truncated border region, the quotients shown in step 2 are not carried out. Instead, a value of 1.0 is entered into the voxels of this border, within the temporary 3D data array that otherwise holds this quotient. Typical border widths are 3–10 \times the Rayleigh resolution width d_{xy} (e.g., 0.75–2.5 μm for $d_{xy} = 0.25 \mu\text{m}$) at the faces along x or y , and on the order of 3–5 Rayleigh DOF's d_z (e.g., 1.5–2.5 μm for $d_z = 0.5 \mu\text{m}$).

Step 3 enforces powerful yet reasonable constraints on the solution of the PSF. As discussed later, it is this important component that makes unambiguous blind deconvolution feasible.

The system also needs a quantitative criterion for stopping the iterations. Several quantitative stopping criteria have been studied for applications in nuclear medicine with varying success (Llacer and Veklerov, 1989; Veklerov and Llacer, 1987), but for microscopy studies, we choose an arbitrary iteration number between 50 and 1,000. The actual number chosen depends upon the amount of noise present in the data and on the amount of time available. Deblurring starts to become substantial at around 50 iterations (see Table 1), but it may continue to improve up to 1,000 iterations (see Table 1), when the data are relatively noise-free (Krishnamurthi *et al.*, 1994). This issue is discussed later under Future Directions.

Wide-Field Fluorescence Algorithm

Figure 2 outlines the constraints on the PSF for WFF and BF referred to in step 3 of Fig. 1. The design of this flowchart is modeled after the original Gerchberg-Saxton approach (Gerchberg and Saxton, 1974). It has the important advantage of being both simple and modular in design, and this simplifies implementation,

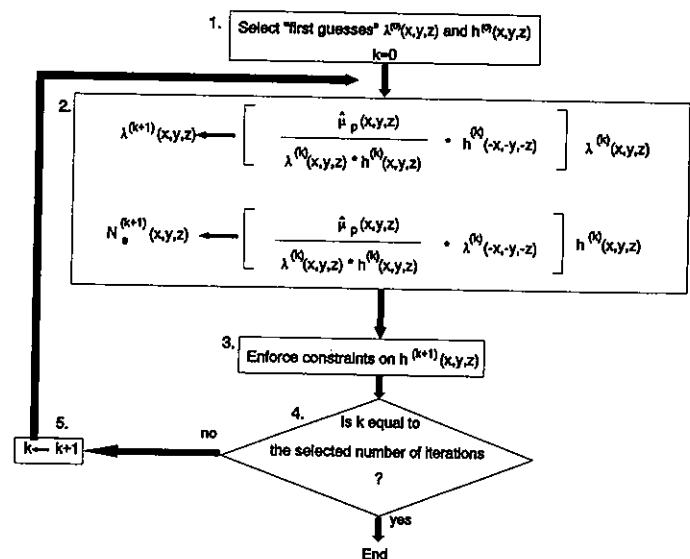


FIGURE 1. General flowchart of the MLE blind deconvolution algorithm: $\lambda^{(k)}(x,y,z)$ is the reconstructed dye concentration of the k -th iteration, $h^{(k)}(x,y,z)$ is the reconstructed PSF of the k -th iteration, $\mu_p(x,y,z)$ is the optically sectioned image data, after being corrected for nonuniform sensitivity and shutter-speed instability, $N_e^{(k)}(x,y,z)$ is the temporary data array that stores an unconstrained form of the estimate of the PSF, during iteration k . Note that this unconstrained estimate is later modified, as indicated, to generate $h^{(k+1)}(x,y,z)$ having the specified constraints.

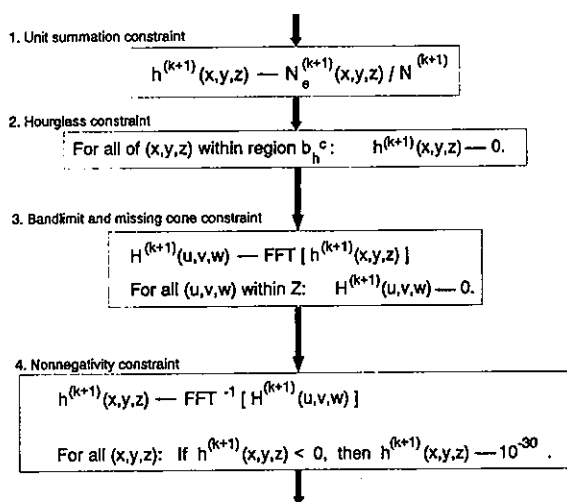


FIGURE 2. Flowchart of constraints applied in WFF and BF. These blocks are substituted for step 3 in Fig. 1 and b_h^c is the complement of b_h . This complement region is the region wherein $h()$ is known to be close to zero, $H^{(k+1)}(u,v,w)$ is the Fourier transform of $h^{(k+1)}()$; Z is the region of the OTF (i.e., $H()$), which is known to be zero; FFT indicates Fast Fourier transform and FFT^{-1} indicates inverse fast-Fourier transform.

adaptation, and refinement. Although it does not conform as rigorously to the EM algorithm as we would like, we have experimental evidence that it does cause an increase in the likelihood values as the iterations proceed (Holmes, 1992; Krishnamurthi *et al.*, 1994), and this implies that it does provide an ML estimate.

Step 1 of Fig. 2 enforces a unit summation constraint on the PSF. Step 2 constrains the energy of the PSF to lie within an hourglass-shaped region that is illustrated in Fig. 3. This constraint prevents portions of the background intensity $b()$ from being erroneously assigned as having originated from the PSF, because it suppresses most of the erroneous background occurring in the region outside the hourglass region. In the 2D diffraction-limited case, discussed later, where the objective of the deblurring algo-

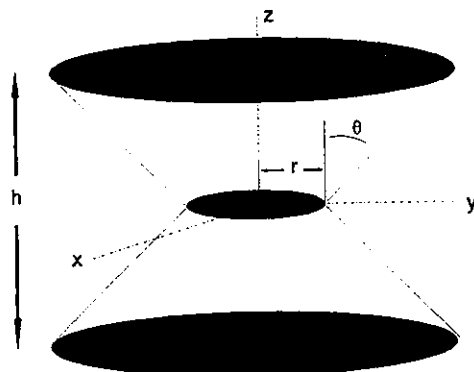


FIGURE 3. Illustration of the hourglass region used in constraining the 3D PSF solution. The term b_h^c denotes the region outside the hourglass. The term h denotes the height spanned in the z -direction by the data array. The radius r is set to be a number (c) of Airy disk widths according to: $r = 0.61c\lambda/\text{NA}$. We have consistently used $c = 3$ because the PSF has very little energy beyond the first three Airy disk widths. The acceptance angle is found from $\theta = \sin^{-1}(\text{NA}/\eta)$, where η is the refractive index.

rithm is to improve the 2D spatial resolution, the acceptable region is a circle with radius r as in Fig. 3.

Step 3 forces the optical transfer function (OTF) to be bandlimited. For the 3D case, the OTF has a frequency band (BW) wherein it may be nonzero, with a missing cone region illustrated in Fig. 4. Step 4 ensures nonnegativity since Step 3 may cause negative numbers. In the 2D diffraction-limited case, the OTF frequency band is described by the interior of a circle having a radius of BW_{xy} following the same formula as in Fig. 4.

Confocal Fluorescence Algorithm

Figure 5 shows the flowchart of the PSF constraint portion of the confocal fluorescence algorithm. Steps 1 through 3 realize the unit summation constraint and the hourglass constraint. In this case, the hourglass constraint ensures that most of the energy lies within the same hourglass region illustrated in Fig. 3. The approach here involves Lagrange multipliers, a one-step late iteration (Lange, 1990) and a Newton-Raphson iteration (step 1; Krishnamurthi *et al.*, 1994). This is more mathematically rigorous compared to the algorithm of Fig. 2 and is needed because the simpler Gerchberg-Saxton approach was not successful for the confocal case. This Lagrange multiplier approach may also be used for the WF case. The upper bound v_u , used to constrain the summation (denoted by v) of the complement region b_h^c , is determined by calculating the value of this summation from the theoretically determined PSF (Kimura and Munakata, 1990; Streibl, 1984). While restricting the background level on the PSF solution well, as the Lagrange multiplier approach is designed to do, it still allows wide freedom in the solved shape of the PSF within the region, where most of its energy resides.

Steps 4–6 represent a Gerchberg-Saxton iteration, which provides a bandlimit constraint under the simplifying assumption that the pinhole aperture in front of the PMT is small enough that the microscope is behaving in a fully confocal mode (i.e., the pinhole is very small and, consequently, the signal level is very low; Kimura and Munakata, 1990; Wilson, 1987). Under this somewhat unrealistic assumption, the WF PSF $h_w()$ and the confocal PSF $h_c()$ are related by the expression

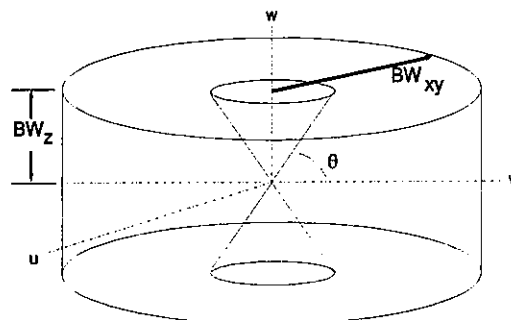


FIGURE 4. Illustration of the region wherein the WF 3D OTF may be nonzero. The 3D coordinates u , v , and w are the frequencies with respect to x , y , and z , respectively. The radial bandlimit follows the formula $\text{BW}_{xy} = 2\text{NA}/\lambda$. The axial bandlimit follows the formula: $\text{BW}_z = (\text{NA})^2/2\eta\lambda$. θ follows the same formula shown in Fig. 3. The biconic region is the "missing cone" region. The region of the OTF where it is known to have all zero values, Z , is the union of this missing cone with the region outside the cylinder.

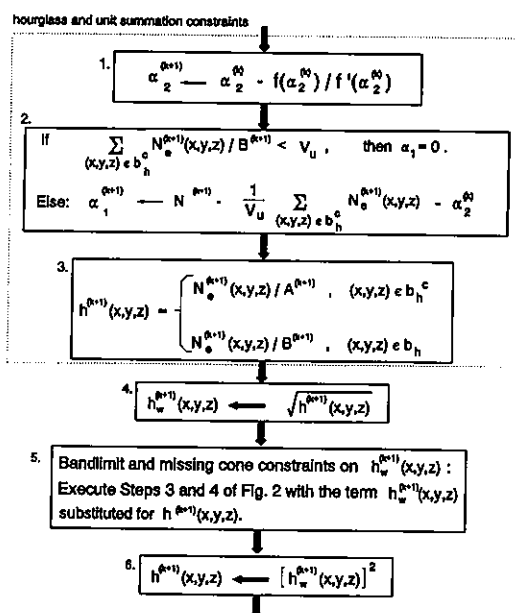


FIGURE 5. Flowchart of the hourglass and bandlimit constraints for the confocal microscope. In addition to enforcing the hourglass constraint, the divisors $A^{(k+1)}$ and $B^{(k+1)}$ inherently constrain the summation of $h^{(k+1)}(x,y,z)$ to be equal to 1. These blocks are substituted for step 3 in Fig. 1.

$$N^{(k)} = \sum_{\text{all}(x,y,z)} N_e^{(k)}(x,y,z)$$

$$A^{(k)} = N^{(k)} - \alpha_1^{(k)} - \alpha_2^{(k)}$$

$$B^{(k)} = N^{(k)} - \alpha_2^{(k)}$$

$$f(\alpha_2^{(k)}) = -1 + \frac{1}{A^{(k)}} \sum_{(x,y,z) \in b_h^c} N_e^{(k+1)}(x,y,z) + \frac{1}{B^{(k)}} \sum_{(x,y,z) \in b_h} N_e^{(k+1)}(x,y,z)$$

$$f'(\alpha_2^{(k)}) = -1 + \frac{1}{[A^{(k)}]^2} \sum_{(x,y,z) \in b_h^c} N_e^{(k+1)}(x,y,z) + \frac{1}{[B^{(k)}]^2} \sum_{(x,y,z) \in b_h} N_e^{(k+1)}(x,y,z)$$

$h^{(k+1)}$ is the $(k+1)$ th PSF estimate; $v^{(k+1)}$ is the summation over the region b_h^c (the region outside of the hourglass) of values in $h^{(k+1)}$; v_u is the upper bound on $v^{(k+1)}$, used to constrain $h^{(k+1)}$; $h_w^{(k+1)}(x,y,z)$ is the iterative estimate of the WF component of the confocal PSF estimate.

$$h_c(x,y,z) = h_w^2(x,y,z) \quad (4)$$

As explained later, the background level $b(x,y,z)$ must be calibrated and may be dealt with either by pre-correction or by incorporation within the algorithm iteration. For the confocal case, we incorporate it within the iteration. This is done by replacing the denominator term in the two equations of Fig. 1 with the term:

$$\lambda^{(k)}(x,y,z) * h(x,y,z) + b \quad (5)$$

with b now being treated as a constant.

Brightfield Algorithm

3D image reconstructions of BF images of absorbing stains are easily produced with a simple variation on the WFF algorithm presented above. The two main requirements are that the specimen cannot be fully opaque and that the condenser NA must be near, or larger than, that of the objective lens.

This variation of the algorithms depends on the approximation that the raw BF data $\mu()$ (with noise $N()$ and background $b()$ ignored) follows a simple linear systems model according to:

$$\mu(x,y,z) = B - h(x,y,z) * \lambda(x,y,z) \quad (6)$$

where B is the bright background intensity, which is the spatially uniform level that is seen when no specimen is present, $h()$ is the PSF, and $\lambda()$ is now the spatially distributed absorption coefficient. This approximation follows from Macias-Garza *et al.* (1989) when only geometric optics are considered, from Streibl (1984) (Eq. 28) when the phase contribution to the intensity is ignored, from Erhardt *et al.* (1985) when light emanating from the specimen is approximated as being fully incoherent, and from Sheppard and Gu (1994) when the specimen is considered a weakly scattering object. We noted that by preprocessing this noise-free raw data according to:

$$\mu_p(x,y,z) = B - \mu(x,y,z) \quad (7)$$

we have a new raw data intensity that follows the model

$$\mu_p(x,y,z) = \lambda(x,y,z) * h(x,y,z) \quad (8)$$

which is identical to the model of Eq. 3. This motivated us to attempt a deblurring of BF data as follows. First, we preprocess the noisy raw data as discussed in Cooper *et al.* (1993) and Chapter 13 to arrive at $\hat{\mu}(x,y,z)$, which is considered an estimate of the $\mu(x,y,z)$ in Eq. 6. Then, $\hat{\mu}(x,y,z)$ is preprocessed according to Eq. 7 to produce an estimate of $\mu_p()$ in Eq. 8. This final, preprocessed result is substituted as $\hat{\mu}_p(x,y,z)$ in the flowchart depicted in Fig. 1.

Although, unlike the fluorescent case, the probability distribution of the noise component $N()$ in 3D BF does not strictly follow a Poisson distribution, as is assumed by the algorithm, we have noticed a remarkably good deblurring of the image. We speculate that this may imply that, while it may be important to have some sort of noise as a fundamental assumption, it is not critical to know its probability distribution accurately. In this sense, we are not strictly performing an MLE for the BF case. We are simply using the algorithm for its convenient deblurring properties.

DATA CORRECTIONS

The camera that we have been using is the electrothermally cooled (-35°C) MCD 220 CCD camera (Spectra Source Instruments, Westlake Village, CA). As a trade-off for its low cost, it has only a 192×165 resolution. However, this is sufficient for many applications, and it maintains the linearity, low noise, 12-bit dynamic range, and extreme low-light sensitivity, which characterize larger cooled-CCD cameras (Aikens *et al.*, 1989; Hiraoka *et al.*, 1987).

Image data collected from any cooled-CCD camera must be calibrated for the background level $b(x,y,z)$, nonuniform, pixel

sensitivity $\beta(x,y)$, and the camera exposure time $T(z)$ such that the raw collected data $\mu_r(x,y,z)$ are composed of:

$$\hat{\mu}_r(x,y,z) = \beta(x,y)T(z)\mu(x,y,z) + b(x,y,z) \quad (9)$$

The exposure time $T(z)$ will vary slightly from frame to frame because of changes in the shutter speed of several milliseconds. The method we use to correct these parameters is outlined by Cooper *et al.* (1993) and is similar to that outlined in Chapter 13.

The corrected data $\hat{\mu}()$ is considered to be an estimate of $\mu()$. For BF, this estimate is then further processed by Eq. 7, to produce $\hat{\mu}_p()$ and for WFF, $\hat{\mu}()$ is substituted for $\hat{\mu}_p()$ in Fig. 1. One advantage of precorrecting the data, as we currently do with the two WF modalities, is that doing so provides a nicely modularized design of the computer algorithm that facilitates their expeditious adaptation to different microscope modalities. In addition, precorrected data consume less computer memory, since the 3D arrays for $b()$ and $\beta()$ do not have to be retained during the deblurring process.

It is also possible to incorporate the calibrated terms $\beta()$, $b()$, and $T()$ directly into the underlying mathematical model, as has been proposed for astronomical and nuclear medicine applications (Politte and Snyder, 1991; Snyder *et al.*, 1993). This has the advantage of better adhering to a Poisson random-point-process model and should ultimately result in improved quantitation of fluorescence concentrations (Politte and Snyder, 1991); we presently incorporate b in this way only with confocal data.

Because in confocal data, $\beta()$ and $T(z)$ are irrelevant, only the $b()$ term must be determined. To estimate b , we simply select a region of interest that appears to not contain any features and then calculate the average background level in this region, as explained later. This average is substituted for b in Eq. 5.

IMAGE RECONSTRUCTIONS

A number of simulated image reconstructions have been carried out in the process of implementing and testing these computer programs. Although not exhaustive, these tests have been instructive because the original "test object data set" is a known

parameter. They give the reader insight into both the advantages and limitations of the technique.

As mentioned, first guesses $\lambda^{(0)}()$ and $h^{(0)}()$ are needed to seed the algorithm. Over the years, we have improved the first-guess strategies, so the data sets presented here use different first-guess strategies. Details are found in the cited literature.

Our present working strategy is as follows. In both WF and BF, we ordinarily use the original optically sectioned data (after correction) as $\lambda^{(0)}()$. Any extended border regions, described in the General Flowchart section, are filled as described by Willis *et al.* (1993, section 4.2). For $h^{(0)}()$, we use a simple constant valued array of value $1/n_{\text{vox}}$, where n_{vox} is the number of voxels. This strategy was used for all of the WF data sets. In the confocal case, for $\lambda^{(0)}()$, we use a simple array having a constant value equal to the average of the original collected data. This is a better choice when the data are especially noisy, as is often the case with confocal data. For $h^{(0)}()$ we use a 3D gaussian function that has full-width half-maximum (FWHM) parameters much broader than the expected PSF. For instance, for the human fibroblast microtubules reconstructed in Figure 11, $h^{(0)}()$ had FWHMs of 1.0 μm in x and y and of 2.0 μm in z , compared to the theoretical FWHMs (Bertero *et al.*, 1990) of 0.17 μm in x and y , and 0.43 μm along z .

Simulated Wide-field Fluorescence

Figure 6 shows a WFF simulation. The test object represents a realistic case where a variety of intensity levels may be expected. The accelerated version of the nonblind algorithm was used. The PSF was assumed the same as that calculated according to diffraction theory (Streibl, 1984). The background $b()$ and sensitivity $\beta()$ functions were not considered.

The seven gray levels in the horizontal bars and the dark rectangle in the center are all distinguishable in Fig. 6c after just 100 iterations. While additional deblurring occurs after more iterations, it is important to emphasize that such high iteration numbers are not always necessary.

Figure 7 shows a projectional side view of another simulation, similar to the one described above but under different conditions and using the earlier, nonaccelerative algorithm and a known PSF. This test object contains a variety of geometric substructures

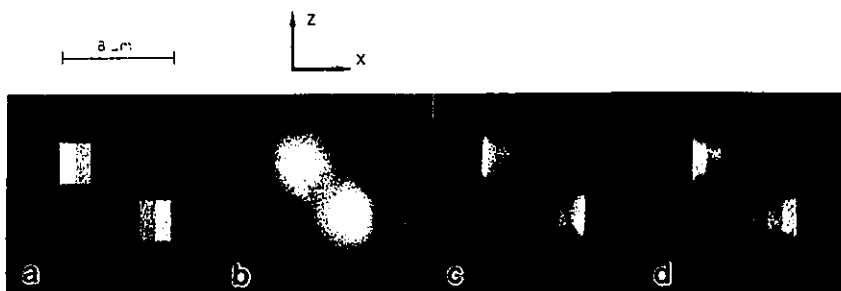


FIGURE 6. Simulation of a 3D image reconstruction from a WFF microscope. The images represent lateral summed projectional views (summed xz views) of a 3D image. (a) The original object to be reconstructed, 8.4 μm (84 pixels) wide by 10 μm (100 pixels) high. (b) Lateral projection image after optical sectioning with an average of 64,000 photons/pixel in this summed, 2D projection, $\lambda = 525 \text{ nm}$, and $\text{NA} = 0.9$. The image data shown are held in a 256×256 pixelated array, with only the central $\sim 190 \times 190$ portion shown. As such, the full 3D data being simulated, in effect, have dimensions of $256 \times 256 \times 256$, and thereby equivalently have about $64,000/256 \approx 250$ photons actually detected/pixel in each image plane, on average. This is a reasonable-to-low count level. The maximum photon count readable by the MCD 220 camera is 150,000 photons/pixel, and typical photon counts may be thousands/pixel. The flat gray border is the region wherein the data are considered to be truncated, as explained earlier. (c,d) Reconstructed images at 100 and 1,000 iterations, respectively.

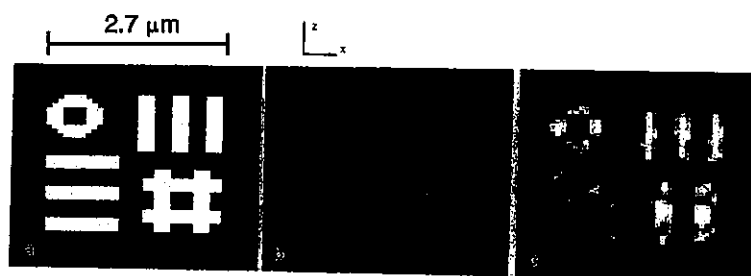


FIGURE 7. Simulation of a 3D image reconstruction from a WFF microscope. The images represent lateral summed projectional views of a 3D image (summed xz views). (a) The original object to be reconstructed, $\sim 2.7 \mu\text{m}$ (27 pixels) wide by ~ 2.7 (27 pixels) high. (b) Lateral projection image after optical sectioning with an average of 1,000 photons per pixel, $\lambda = 525 \text{ nm}$ and $\text{NA} = 0.9$. The image data shown were held in a 64×64 pixelated array, with the central $\sim 45 \times 45$ portion shown. In effect, the full 3D image being emulated has dimensions of $64 \times 64 \times 64$ and therefore represents the detection of $1,000/64 = 15.6$ photons per data voxel, on average. This is a lower than typical count level with a cooled-CCD camera. (c) Reconstructed image with the nonaccelerated nonblind, algorithm after 1,000 iterations.

that are somewhat sparse, in that there is no fluorescence between each substructure.

One type of geometry seems difficult to reconstruct precisely. In the lower left-hand corner there are 3 horizontal, parallel planar objects whose arrangement is distorted in the reconstruction. This distortion is more severe because the spacing of these planar substructures is so close to the resolution limit, just $0.6 \mu\text{m}$ apart in z compared to a Rayleigh $\text{DOF} = 0.5 \mu\text{m}$.

We expect that any of the other current 3D image reconstruction algorithms will have difficulty in reconstructing a test object of this type, but errors of this type place some limits on the classes of structures that can be reconstructed precisely. This limitation is not too restrictive, because most biological anatomy is not horizontally planar with a uniform fluorescence. Even a confocal microscope has difficulty in accurately imaging this geometry, unless it is used in conjunction with 3D image deblurring.

simulation was carried out as a vehicle for debugging a computer algorithm for use when background intensity effects are present. For details, see Krishnamurthi *et al.* (1992).

The algorithm of Figures 1 and 5 was used, with the constraints implemented as follows: The v_u constraint was implemented according to Figure 5, but with steps 4–6 (for confocal only) replaced by steps 3 and 4 of Figure 2. As the theoretical summation v in the b_h^c region was calculated from the theoretical PSF to be 0.0518, the v_u upperbound was then set to 0.06 to allow for some margin. A constant background level $b()$ was assumed to be known and $\cong 13\%$ of the peak intensity level in the image (including the intrinsic Poisson noise) although, with real data, this background level would have to be measured as outlined above. This b term was used with Eq. 5 to replace the denominator terms in Figure 1.

Simulated 2D Diffraction-Limited Wide-field Fluorescence with Blind Deconvolution

Figure 8 shows a simulation of a blind deconvolution on 2D diffraction-limited data to improve the spatial resolution. This

Wide-field Fluorescence Biological Sample

Figures 9 and 10 show images obtained by WFF of DNA labeled with acriflavin using a sample from the hippocampus of a rat brain.

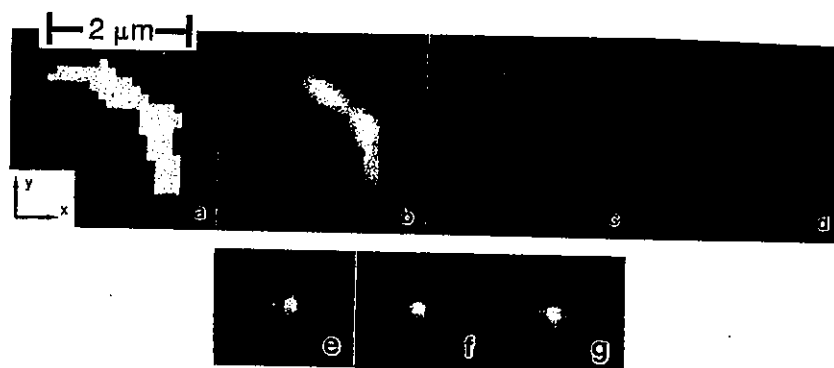


FIGURE 8. Simulation of a 2D diffraction-limited image reconstruction from a WFF microscope. (a) The original object to be reconstructed, $2 \mu\text{m}$ (16 pixels) wide by $2 \mu\text{m}$ (16 pixels) high. (b) Diffraction-limited image with an average of 4,000 photons/pixel and a peak intensity of $\sim 27,000$ photons/pixel, $\lambda = 525 \text{ nm}$, a $\text{NA} 1.0$ lens, and a background level that is, on average, $\sim 13\%$ of the peak intensity. Both the foreground and background photon counts were randomized to emulate Poisson photon-counting statistics. The data were held in a 64×64 pixelated array with only the central $\sim 22 \times 22$ portion shown. (c, d) Reconstructed images from the blind deconvolution algorithm at 50 and 500 iterations, respectively. (e) True PSF, an Airy diffraction pattern. (f, g) Reconstructed PSFs from the blind deconvolution algorithm at 50 and 500 iterations, respectively.

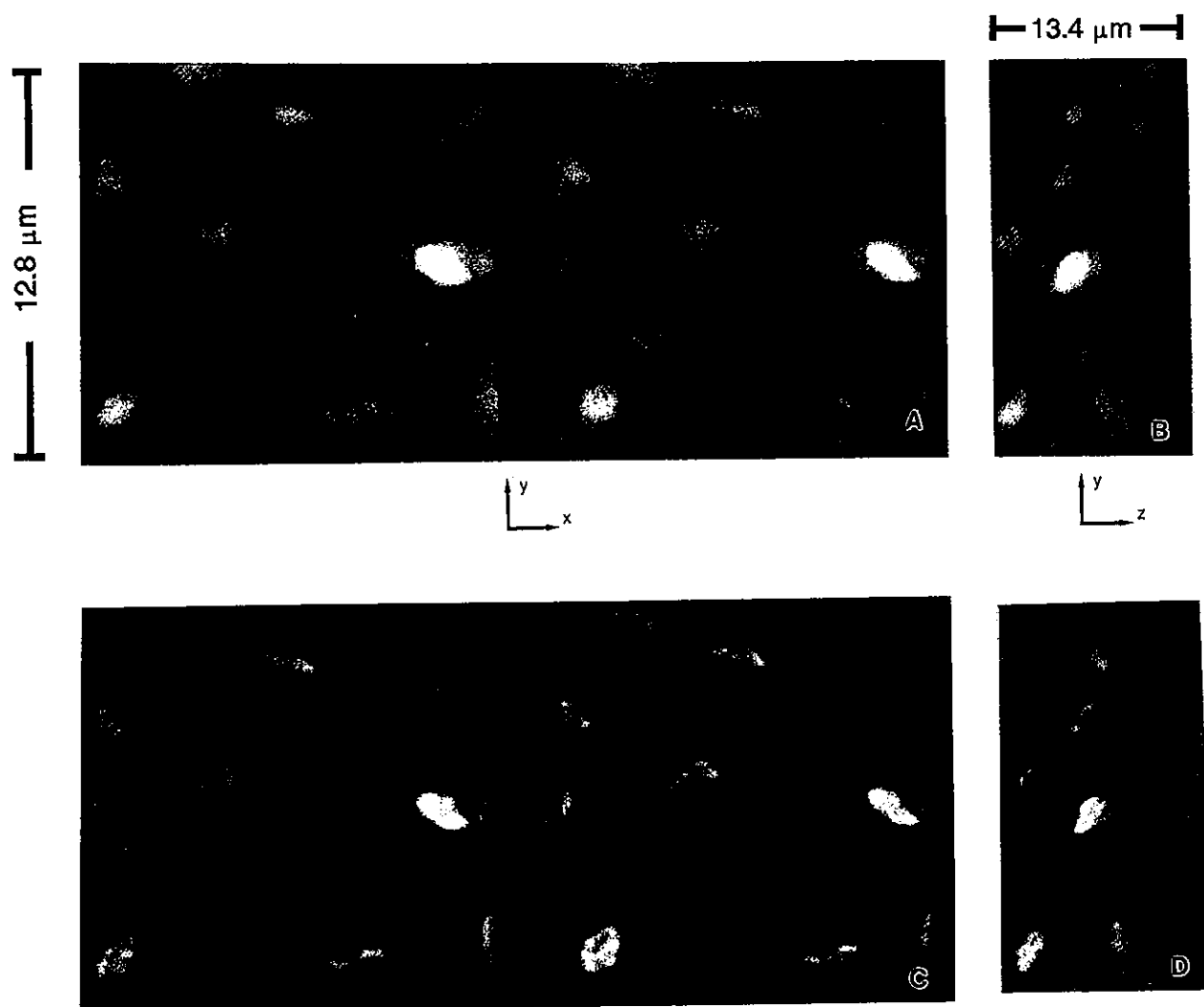


FIGURE 9. Wide-field fluorescent 3D data of nuclei from the hippocampus of a rat brain. The nuclei are labeled with acriflavin (Kasten, 1993). (a) Stereo-pair of the original unreconstructed data after being corrected according to Cooper *et al.* (1993) and Chapter 13, *this volume*. Field size $15.4 \times 12.8 \times 13.4 \mu\text{m}$ (x, y, z); sampling $128 \times 128 \times 64$ (x, y, z); spectra source MCD 220 cooled-CCD camera; $100\times$, NA 1.25 oil lens. The data were rendered by **maximum intensity projections** with the ANALYZE software (Mayo Foundation, Rochester MN). (b) Side view (x, z) of the data in (a). (c) Reconstructed by MLE after 600 iterations. Borders of size 0.93 , 0.81 , and $1.86 \mu\text{m}$ were used at each of the two faces along x , y , and z , respectively. Note the haze removal and better visualization of nuclear texture. Both image sets had their gray levels similarly modified by the γ correction feature of the XV public-domain image-processing software (John Bradley, University of Pennsylvania), in order to visualize the low-intensity features. Some of the nuclei had low intensities and were difficult to see without a gamma correction. The vertical stripes are a 3D-rendering artifact of voxels that straddle the last plane and are not associated with blind deconvolution. (d) Side view of the data in (c).

Reconstructed 3D data sets of this sort can be used to assess qualitatively the distribution of cells in tissue as a function of development, disease or insult due to neurotoxic compounds. Automatic quantitative analysis based on 3D segmentation methods (Cohen *et al.*, 1994; Roysam *et al.*, 1994) are possible as well.

Figure 10 shows summed projectional views of the reconstructed PSF showing the expected biconic shape.

Confocal Fluorescence Biological Samples

Figures 11 and 12 show images that were obtained from a confocal fluorescence microscope, with and without deblurring. Here, we are imaging bundles of microtubules in human fi-

broblasts, structures that are significantly narrower than the Rayleigh resolution of the microscope.

The total processing time was just under 2 min. The first guess of the PSF was chosen to be a 3D Gaussian function having FWHM parameters of $1.0 \mu\text{m}$ in x and y , and $2.0 \mu\text{m}$ in z (again, much broader than the expected PSF dimensions).

Note the apparent improvement in signal-to-noise in the reconstructed images when compared to the raw images. Many of the microtubules become surprisingly more visible. As explained earlier, this is possible because the data are sampled at a rate higher than the Nyquist rate. Residual out-of-focus haze is also further reduced, as is the overall axial smearing.

The value of the upperbound v_u on the summation v in the b_h region was selected as follows. The theoretical PSF was calcu-

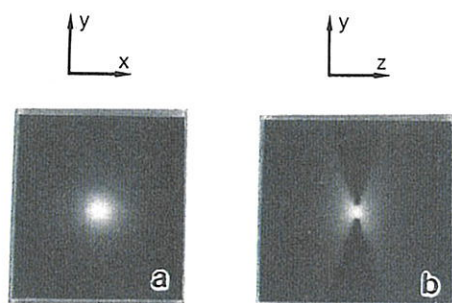


FIGURE 10. Summed intensity projections of the PSF reconstructed from the same data as that of Fig. 9 after 600 iterations. (a) Top projection. (b) Side projection (x,z view). Only the central portion is shown. Note that it shows the expected flaring characteristic of light spreading in out-of-focus planes; γ was nonlinear, to emphasize low-intensity details.

lated according to Kimura and Munakata (1990) and, from this, the **theoretical** summation ν was found to be 0.03. To be safe, we constrained the **reconstructed** ν to be <0.06 (i.e., $\nu_u = 0.06$). The background $b()$ for Eq. 5 was estimated to be the average of a "blank" $150 \times 150 \times 50$ section in the original $512 \times 512 \times 50$ data. As indicated, a $64 \times 64 \times 50$ segment was taken from the $512 \times 512 \times 50$ data and then was augmented to a $64 \times 64 \times 64$ array for deblurring.

Figure 13 shows a set of images from another confocal data set (Krishnamurthi *et al.*, 1992, 1994). In this case, axial smearing is substantially reduced, and the structure is much clearer in the final image, which was reconstructed in the same way as that in Figure 12.

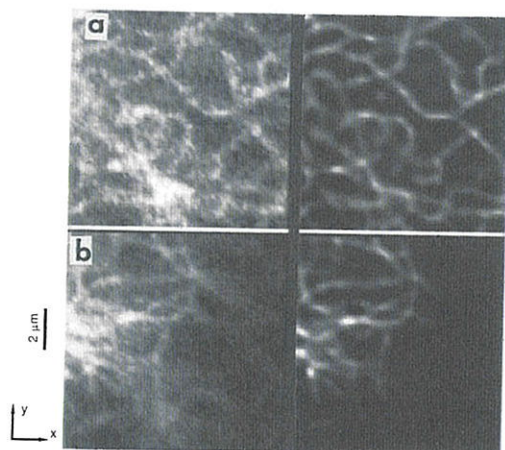


FIGURE 11. Two raw confocal sections near the center of a set of fibroblast microtubules labeled with anti- β -tubulin/FITC (left). Sarastro CLSM 2000N upright microscope (Molecular Dynamics, Sunnyvale, CA); $60\times$, NA 1.4 Nikon Planapo lens; $\lambda_{ex} = 488$ nm; $\lambda_{em} = 510$ nm; field size $10.8 \times 10.8 \times 4.9$ μm (x,y,z); sampling $64 \times 64 \times 50$ (x,y,z); physical pinhole diameter = 50 μm , or 0.22 μm at the object plane. The optical sections were augmented in z by adding 7 extra sections for later truncation to both ends, to a $64 \times 64 \times 64$ raw data array. No border was used in the x or y dimensions.

These two optical sections are separated by 1.56 μm , although the sample was scanned at 0.098 - μm intervals. The raw confocal data are noisy. The reconstructed images (right) were obtained after just 50 iterations of the blind deconvolution algorithm.

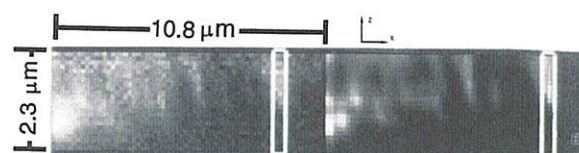
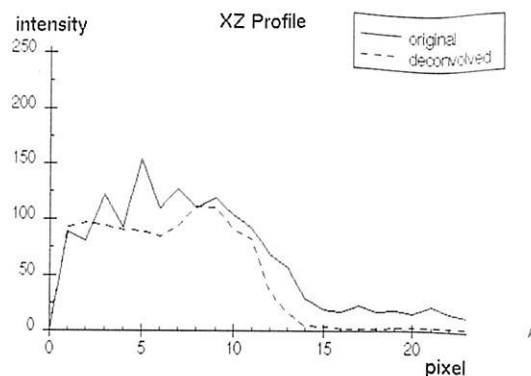


FIGURE 12. Vertical cross section through the 3D data sets described in Fig. 11. Original (left) and reconstructed after 50 iterations (right). Only the central 23 optical slices are shown. Each image was generated by applying a maximum-intensity projection to four vertical slices. In other words, the maximum value among four horizontally adjacent voxels near the center of the 3D data array was taken. The plot shown is a profile taken of the region of interest shown in the photographs. This profile represents the average of the two adjacent pixels that the short axis of this region spans. In other words, each value in the plot is the average value of the two horizontally adjacent pixels marked by the region of interest. Note the apparent noise reduction. The reconstructed data show a sharper drop in intensity at about pixel number 12, implying improved axial definition.

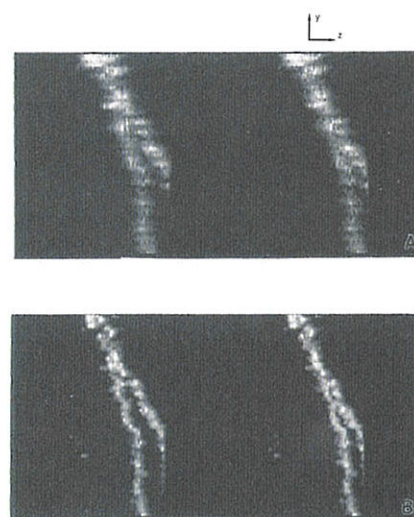


FIGURE 13. Lateral maximum-intensity stereo projection of a rat hippocampus dendritic field labeled with Lucifer Yellow. Olympus BH-2 microscope, BioRad MRC-600 confocal scan box; field size $50 \times 50 \times 26$ μm (x,y,z); sampling $64 \times 64 \times 64$; $20\times$, NA 0.8 oil lens; physical PMT pinhole diameter = 1.0 mm in detector plane, 0.94 μm at object plane. (a) Raw data rendered by maximum intensity projection, using ANALYZE software. (b) Reconstruction showing axial deblurring and noise reduction after 1,000 iterations.

Brightfield Biological Sample

Figures 14 and 15 show images obtained by BF microscopy. A pyramidal neuron in a 500 μm thick slice of neonatal rat hippocampus was injected with biocytin and contrasted with avidin/horseradish-peroxidase reacted with diaminobenzidine (Deitch *et al.*, 1991). Note the substantial improvement after just 100 iterations (Fig. 15c,d). This would be sufficient if, for example, one were just interested in the arrangement of the dendrites and not the dendritic spines. If one is interested in even finer detail, such as the spines, a higher iteration number is needed as shown in Figure 15e,f. Figure 16 shows the reconstructed PSF.

FUTURE DIRECTIONS

It is our understanding that other model-based optimization approaches, such as a least-squares approach (Carrington, 1990), provide similar noise suppression. It is possible that one could extend such model-based approaches to incorporate blind deconvolution and, following the preprocessing of Eq. 7, to use them to reconstruct BF micrographs. Limited independent computer-simulated comparisons have demonstrated that model-based MLE and least-squares approaches perform better at suppressing noise and avoiding artifacts in comparison to some non-model-based approaches (Conchello and Hansen, 1990; Fay *et al.*, 1989) and future refinements ought to make them even more robust. In the future, blind deconvolution methods may apply bayesian techniques to further reduce noise and improve deblurring (Joshi and Miller, 1993; Lalush and Tsui, 1992).

The most obvious factor limiting the more widespread use of deconvolution techniques is computer execution time. This will vary with the computer, the image dimensions, and the number of

iterations. Table 1 summarizes some benchmarks as of 1994. Also, as the accelerated version of the nonblind algorithm resulted in a $\sim 7\times$ increase in overall convergence speed, we may expect a similar improvement when this approach is applied to the blind deconvolution. When just stereo-pairs are sufficient for viewing the specimen, one can apply a simple version of the MLE-based algorithm, of which 50 iterations will execute in ~ 9 sec, using the i860 accelerator card discussed in the Table 1 footnote (Holmes *et al.*, 1991).

Fast 3D imaging, with speeds approaching that needed for real-time viewing, is likely to be developed in the future. Computer speed and cost continue to improve remarkably every year. Even with currently available computer and electronic components, it is possible to build a system that will deconvolve MLE stereo-pairs (Holmes *et al.*, 1991) in near-real time. Based on computer manufacturer specifications, 50 iterations of a 2D version of the MLE nonblind algorithm on 256×256 images should require ~ 9 sec on an Alacron i860 card.

A second limitation is that the algorithm is sometimes unstable when taken out to a very high number of iterations ($\sim 10,000$). The instability generates a severe "salt-and-peppery" noise artifact, which is attributed to an instability that is inherent in estimating point process densities (Miller and Snyder, 1987). It is not due to our specific implementation and has been observed with other deblurring algorithms (Conchello and Hansen, 1990). We have had some success in adapting the Method of Sieves to remove this effect as originally proposed by Snyder *et al.* (1987) for nuclear medicine imaging. However, from a practical standpoint, it is easier to stop the iteration before the artifact appears. The artifact is obvious and easy to identify, so it is straightforward to store the solutions at, say, 50, 200, and 500 iterations, and then to choose the one that occurs just before the artifact is detectable.

Researchers in nuclear medicine have proposed quantitative stopping criteria, based on a calculation of the chi-square parameter, with varying success (Hebert *et al.*, 1988; Llacer and Veklerov, 1989). A stopping criterion will be advantageous in two ways: it is likely to eliminate the guesswork in choosing the number of iterations making the results more repeatable, and it would regularize the reconstruction so as to prevent the occurrence of the noise artifact.

A third limitation exists in the sizes of images that are possible today. Table 1 implies that $128 \times 128 \times 64$ images are quite practical. $256 \times 256 \times 64$ images are possible, but computer memory and execution time will increase roughly proportionate to this size (see Table 1 caption). $512 \times 512 \times 128$ images are not realistic with WF data today, although this will change with faster computers, extra memory, and faster algorithms. As confocal data sets as large as $512 \times 512 \times 128$ are typical, speed and larger array size are advantages that this approach has over WF imaging with deblurring.

Related image analysis and enhancement techniques that employ MLE include automation of noise removal (Roysam *et al.*, 1992), cell counting (Roysam *et al.*, 1994), morphometric feature measurements, and neuron tracing (Cohen *et al.*, 1994). Figure 17 illustrates automatic noise removal. Ideally, these analysis and enhancement techniques should be merged with deblurring algorithms to produce a single unified algorithm that deconvolves, removes noise, and measures morphometric features, simultaneously.

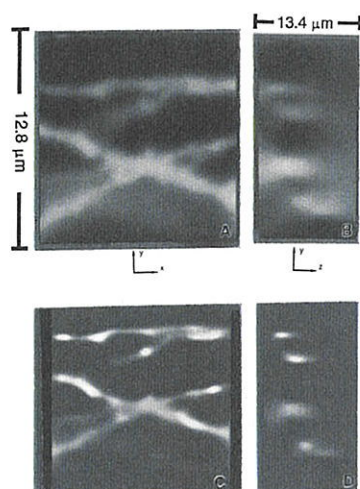


FIGURE 14. Cross sections through the optically sectioned dendritic field. (a) and (b) are without image reconstruction, but after being corrected as described in Cooper *et al.* (1993; Chapter 13, this volume) and after further pre-processing according to Eq. 7. Details are as follows: field size $15.4 \times 12.8 \times 13.4 \mu\text{m}$ (x,y,z); sampling $128 \times 128 \times 64$ (x,y,z); spectra source MCD 220 cooled-CCD camera; Gray levels are inverted. (a) Central x,y cross section, showing out-of-focus blur. (b) Central y,z cross section. (c,d) The same cross sections, respectively, after 100 iterations of the blind deconvolution.

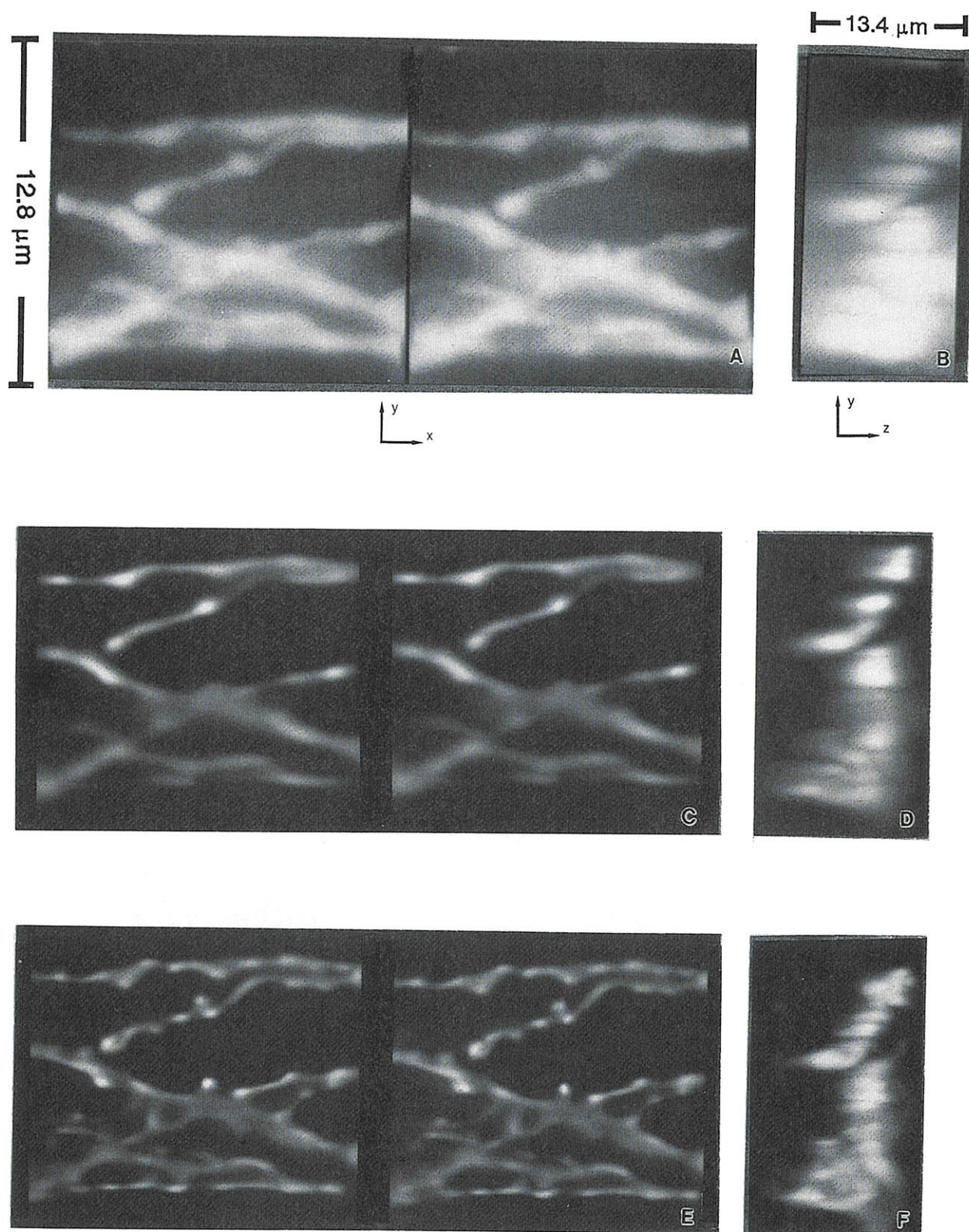


FIGURE 15. Stereo-pairs, looking down the optical axis by maximum intensity projection, and lateral projections of the BF data set of Fig. 14. (a,b) Original unreconstructed data. (c,d) Reconstruction at 100 iterations. (e,f) Reconstruction at 600 iterations.

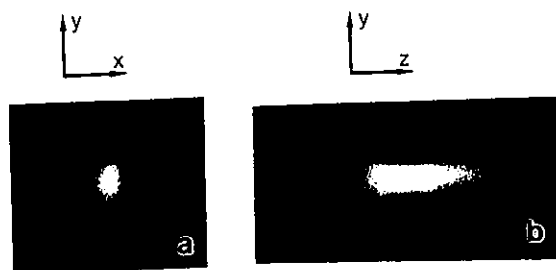


FIGURE 16. Summed intensity projections of the PSF reconstruction corresponding to Fig. 14 after 600 iterations. (a) Top projection. (b) Side projection. The apparent acceptance angle is narrower than that calculated from the NA but appears to be consistent with the apparent acceptance angle seen in cross sections of the raw data, as in Fig. 14b. γ was modified to show the low-intensity details. Only the central portion of the data set is shown.

SUMMARY OF MAIN POINTS

- The MLE approach to deblurring has a number of important advantages—no measurement of PSF needed and inherent noise suppression (provided data originally over-sampled and number of iterations is constrained to 1,000).
- This approach has been adapted for three separate microscope modalities: (1) WFF, (2), confocal fluorescence, and (3) transmitted light BF.
- Present limitations are in computation speed (see Table 1), maximum possible array size and (when taken out to well over 1,000 iterations) a noise artifact at very high iteration numbers. All 3D deblurring algorithms have these limitations to some extent, but future refined versions ought to address them.

ACKNOWLEDGMENTS

This research was supported in part by grants from the National Science Foundation (BCS-9011701), the Whitaker Foun-

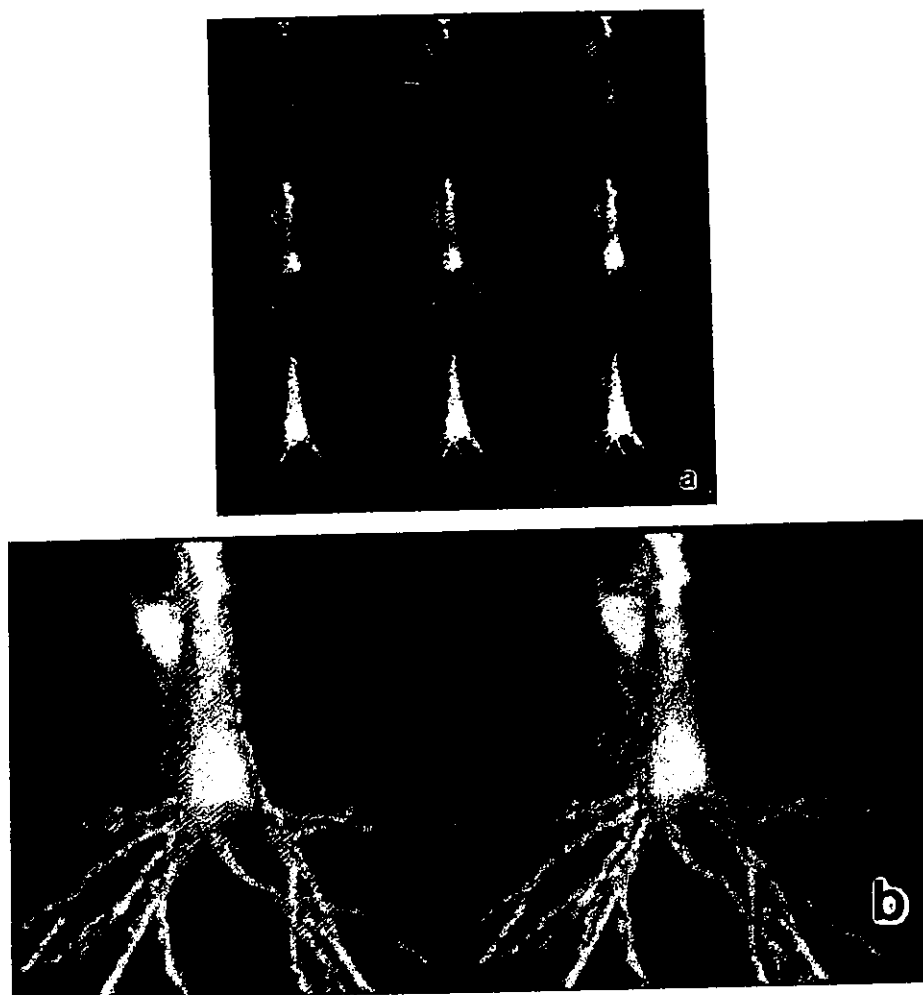


FIGURE 17. (a) Set of sequential raw confocal image slices showing background noise. The sections represent the soma and a portion of the dendrites of a CA₃ hippocampal pyramidal cell from the brain of a rat. Field width = 500 μm ; sampling of 128 \times 128. A total of 30 successive slices were collected 1 μm apart. Not all the slices are shown. For details, see Roysam *et al.* (1992). (b) A surface projection stereo-pair of the intensity estimate obtained using the MLE-based noise removal algorithm presented in Roysam *et al.* (1992). Note the substantial reduction in noise and improved contrast while maintaining the continuity of the dendrites.

dation, and the National Institutes of Health (1R55RR0690401). Computer and other resources were provided, in part, by the Center for Image Processing Research at Rensselaer (NSF grant CDA-8805910) and by the Cornell National Supercomputer Facility, which receives major funding from the NSF, IBM and New York State.

REFERENCES

- Agard, D.A., 1984, Optical sectioning microscopy: Cellular architecture in three dimensions, *Annu. Rev. Biophys. Bioeng.* 13:191-219.
- Aikens, R.S., Agard, D.A., and Sedat, J.W., 1989, Solid-state imagers for microscopy, *Methods Cell Biol.* 29:291-313.
- Ayers, G.R., and Dainty, J.C., 1988, Iterative blind deconvolution method and its applications, *Optics Lett.* 13:547-549.
- Bertero, M., Boccacci, P., Brakenhoff, G.J., Malfanti, F., and van der Voort, H.T.M., 1990, Three-dimensional image restoration and super-resolution in fluorescence confocal microscopy, *J. Microsc.* 157:3-20.
- Carrington, W.A., 1990, Image restoration in 3D microscopy with limited data. Bioimaging and two-dimensional spectroscopy, Los Angeles, *Proc. Int. Soc. Opt. Eng.* 1205:72-83.
- Cohen, A.R., Roysam, B., and Turner, J.N., 1994, Automated tracing and volume measurements of neurons from 3-D confocal fluorescence microscopy data, *J. Microsc.* 173:103-114.
- Conchello, J., and Hansen, E., 1990, Enhanced 3-D reconstruction from confocal scanning microscope images. 1. Deterministic and maximum likelihood reconstructions, *Appl. Optics* 29:3795-3804.
- Cooper, J.A., Bhattacharyya, S., Turner, J.N., and Holmes, T.J., 1993, Three-dimensional transmitted light brightfield imaging: Pragmatic data collection and preprocessing considerations. In: *Microscope Society of America Annual Meeting, Cincinnati*, San Francisco Press, 51:276-277.
- Deitch, J.S., Smith, K.L., Swann, J.W., and Turner, J.N., 1991, Ultrastructural investigation of neurons identified and localized using the confocal scanning laser microscope, *J. Electron Microsc. Technique* 18:82-90.
- Dempster, A.P., Laird, N.M., and Rubin, D.B., 1977, Maximum likelihood from incomplete data via the EM algorithm, *J. R. Stat. Soc. B* 39:1-37.
- Erhardt, A., Zinser, G., Komitowski, D., and Bille, J., 1985, Reconstructing 3-D light-microscopic images by digital image processing, *Appl. Optics* 24:194-200.
- Fay, F.S., Carrington, W., and Fogarty, K.E., 1989, Three-dimensional molecular distribution in single cells analysed using the digital imaging microscope, *J. Microsc.* 153:133-149.
- Gerchberg, R.W., and Saxton, W.O., 1974, Super-resolution through error energy reduction, *Optica Acta* 21:709-720.
- Gibson, S.F., and Lanni, F., 1991, Experimental test of an analytical model of aberration in an oil-immersion objective lens used in three-dimensional light microscopy, *J. Opt. Soc. Am. A* 8:1601-1613.
- Hebert, T., Leahy, R., and Singh, M., 1988, Fast MLE for SPECT using an intermediate polar representation and a stopping criterion, *IEEE Trans. Nucl. Sci.* 35:615-619.
- Hiraoka, Y., Sedat, J.W., and Agard, D.A., 1987, The use of charge-coupled device for quantitative optical microscopy of biological structures, *Science* 238:36-41.
- Hiraoka, Y., Sedat, J.W., and Agard, D.A., 1990, Determination of three-dimensional imaging properties of a light microscope system: Partial confocal behavior in epifluorescence microscopy, *Biophys. J.* 57:325-333.
- Holmes, T.J., 1989, Expectation-maximization restoration of band-limited, truncated point-process intensities with application in microscopy, *J. Opt. Soc. Am. A* 6:1006-1014.
- Holmes, T.J., 1992, Blind deconvolution of quantum-limited incoherent imagery, *J. Opt. Soc. Am. A* 9:1052-1061.
- Holmes, T.J., and Liu, Y.H., 1991, Acceleration of maximum-likelihood image-restoration for fluorescence microscopy and other noncoherent imagery, *J. Opt. Soc. Am. A* 8:893-907.
- Holmes, T.J., Liu, Y.H., Khosla, D., and Agard, D.A., 1991, Increased depth-of-field and stereo pairs of fluorescence micrographs via inverse filtering and maximum likelihood estimation, *J. Microsc.* 164:217-237.
- Janesick, J.R., Elliott, T., and Collins, S., 1987, Scientific charge-coupled devices, *Opt. Eng.* 26:692-714.
- Joshi, S., and Miller, M.I., 1993, Maximum a posteriori estimation with Good's roughness for three-dimensional optical-sectioning microscopy, *J. Opt. Soc. Am. A* 10:1078-1085.
- Kasten, F.H., 1993, Introduction to fluorescent probes: Properties, history and applications. In: *Fluorescent Probes for Biological Function of Living Cells: A Practical Guide* (W.T. Mason and G. Relf, eds.), Academic Press, London, in press.
- Kimura, S., and Munakata, C., 1990, Dependence of 3-D optical transfer functions on the pinhole radius in a fluorescent confocal optical microscope, *Appl. Optics* 29:3007-3011.
- Krishnamurthi, V., Liu, Y., Holmes, T.J., Roysam, B., and Turner, J.N., 1992, Blind deconvolution of 2D and 3D fluorescent micrographs. In: *Biomedical Image Processing III and Three-Dimensional Microscopy*, San Jose, *Proc. Int. Soc. Opt. Eng.* 1660:95-102.
- Krishnamurthi, V., Turner, J.N., Liu, Y., and Holmes, T.J., 1994, Blind deconvolution for fluorescence microscopy by maximum likelihood estimation, *Appl. Optics*.
- Lalush, D.S., and Tsui, M.W., 1992, Simulation evaluation of Gibbs prior distributions for use in maximum a posteriori SPECT reconstructions, *IEEE Trans. Med. Imaging* 11:267-275.
- Lange, K., 1990, Convergence of EM image reconstruction algorithms with Gibbs smoothing, *IEEE Trans. Med. Imaging* 9:439-446.
- Llacer, J., and Veklerov, E., 1989, Feasible images and practical stopping rules for iterative algorithms in emission tomography, *IEEE Trans. Med. Imaging* 8:186-193. errata 9:112, 1990.
- Lucy, L.B., 1974, An iterative technique for the rectification of observed distributions, *Astron. J.* 79:745-765.
- Macias-Garza, F., Diller, K.R., Bovik, A.C., Aggarwal, S.J., and Aggarwal, J.K., 1989, Improvement in the resolution of three-dimensional data sets collected using optical serial sectioning, *J. Microsc.* 153:205-221.
- Martin, L.C., and Johnson, B.K., 1931, *Practical Microscopy*, Blackie and Son, London.
- Miller, M.I., and Snyder, D.L., 1987, The role of likelihood and entropy in incomplete-data problems: Applications to estimating point-process intensities and Toeplitz constrained covariances, *Proc. IEEE* 75:892-907.
- Oppenheim, A.V., and Schaffer, R.W., 1975, *Digital Signal Processing*, Prentice-Hall, Englewood Cliffs, New Jersey.
- Politte, D.G., and Snyder, D.L., 1991, Corrections for accidental coincidences and attenuation in maximum-likelihood image reconstruction for positron-emission tomography, *IEEE Trans. Med. Imaging* 10:82-89.
- Richardson, W.H., 1972, Bayesian-based iterative method of image restoration, *J. Opt. Soc. Am.* 62:55-59.
- Roysam, B., Bhattacharyya, A.K., Srinivas, C., and Turner, J.N., 1992, Unsupervised noise removal algorithms for 3-D confocal fluorescence microscopy, *Micron Microsc. Acta* 23:447-461.
- Roysam, B., Ancin, H., Bhattacharyya, A.K., Chisti, A., Seegal, R., and Turner, J.N., 1994, Algorithms for automated characterization of cell populations in thick specimens from 3-D confocal fluorescence data, *J. Microsc.* 173:115-126.
- Shaw, P.J., and Rawlins, D.J., 1991, Three-dimensional fluorescence microscopy, *Prog. Biophys. Mol. Biol.* 56:187-213.
- Shepp, L.A., and Vardi, Y., 1982, Maximum likelihood reconstruction for emission tomography, *IEEE Trans. Med. Imaging* 1:113-121.
- Sheppard, C.J.R., and Gu, M., 1994, 3D imaging in brightfield reflection and transmission microscopes. In: *3D Image Processing in Microscopy*, Munich, Society for 3D Imaging in Microscopy.
- Snyder, D.L., Hammoud, A.M., and White, R.L., 1993, Image recovery from data acquired with a charge-coupled-device camera, *J. Opt. Soc. Am. A* 10:1014-1023.
- Snyder, D.L., Miller, M.I., Thomas, L.J., and Politte, D.G., 1987, Noise and edge artifacts in maximum-likelihood reconstructions for emission tomography, *IEEE Trans. Med. Imaging* 6:228-238.

- Streibl, N., 1984, Depth transfer by an imaging system, *Optica Acta* 31:1233-1241.
- Turner, J.N., Szarowski, D.H., Smith, K.L., Marko, M., Leith, A., and Swann, J.W., 1991, Confocal microscopy and three-dimensional reconstruction of electrophysiologically identified neurons in thick brain slices, *J. Electron Microsc. Technique* 18:11-23.
- Van Trees, H.L., 1968, *Detection, Estimation, and Modulation Theory*, Wiley, New York.
- Veklerov, E., and Llacer, J., 1987, Stopping rule for the MLE algorithm based on statistical hypothesis testing, *IEEE Trans. Med. Imaging* 6:313-319.
- Visser, T.D., Oud, J.L., and Brakenhoff, G.J., 1992, Refractive index and axial distance measurements in 3-D microscopy, *Optik* 90:17-19.
- Willis, B., Turner, J.N., Collins, D.N., Roysam, B., and Holmes, T.J., 1993, Developments in three-dimensional stereo brightfield microscopy, *Microw. Res. Technique* 24:437-451.
- Wilson, T., 1987, The size of detector in confocal imaging systems, *Optics Lett.* 12:227-229.